ELSEVIER

Contents lists available at ScienceDirect

Extreme Mechanics Letters

journal homepage: www.elsevier.com/locate/eml



Geometric optimization of pillars for enhanced adhesion

Sumukh S. Pande, Kevin T. Turner*

Department of Mechanical Engineering and Applied Mechanics, University of Pennsylvania, Philadelphia, PA 19104, United States



ARTICLE INFO

Article history:
Received 6 November 2022
Received in revised form 11 January 2023
Accepted 22 January 2023
Available online 31 January 2023

Keywords: Geometric optimization Adhesion Free-form pillar Interface failure Dry adhesives

ABSTRACT

Interfaces with enhanced dry adhesion have applications in various fields, including robotic grasping and microtransfer printing. Arrays of pillars or fibers with mushroom-like geometries and variations on these have been used to achieve relatively strong adhesion to a broad range of surfaces via surface forces. Here, we investigate the optimal geometries for adhesive pillars through a gradient-based optimization scheme. The scheme minimizes an objective function based on the strain energy release rate of a crack at the pillar edge. The optimal design yields a stress distribution at the interface that is nearly-uniform and free from edge stress singularities. Experiments were performed on millimeter-scale pillars to evaluate the efficacy of the designs. A maximum adhesion enhancement of 2x was achieved for a pillar with a stalk radius equal to half of the contact radius. The location of crack initiation was shifted to the center of the pillar from the edge, indicating that the optimal design does indeed significantly reduce the stress concentration in the near-edge region. This geometric optimization scheme is versatile and can be extended to other scenarios where the control of stresses through geometry can be used to improve the performance of adhered interfaces and bonded joints.

© 2023 Elsevier Ltd. All rights reserved.

1. Introduction

Dry adhesives exploit surface forces (e.g., van der Waals) and the engineering of interfacial stress states to achieve interfaces with high adhesion and releasability [1]. They have applications in multiple areas, including robotic grasping and climbing [2-6], temporary adhesives [7-10] and microtransfer printing [11-14]. Much of the work on fibrillar adhesives has been inspired by attachment structures found on lizards, notably the gecko, and insects [15,16]. It has been shown that the exceptional adhesive performance of these natural systems is due in part to the spatula-shaped and mushroom-shaped geometries of the individual fibrils [17]. This shape reduces the stress concentration at the edge of the fibril and enhances the pull-off force. Based on this observation, many engineered adhesive structures with mushroom-shaped pillars have been demonstrated; this tip geometry redistributes stresses at the interface such that the stress in the central region increases and the stress concentration at the edge decreases [18-20]. As detachment typically initiates at the edge of the pillar, this reduction in edge stress increases the effective adhesion strength of the pillar. An alternate approach to manipulate the stress distribution via a composite pillar structure with a soft tip and a stiff core has also been demonstrated [21–23]. This configuration results in a reduction of the stress

concentration at the edge, leading to enhanced adhesive performance relative to a homogeneous cylindrical pillar. In addition, various other geometries that employ similar principles to enhance adhesion have been reported [24–26].

To optimize the shape of fibrils/pillars for improved performance, Gao et al. [27] noted that the interfacial stress distribution should be uniform as this would allow the theoretical adhesion strength of the interface to be achieved. There have been multiple efforts to identify a pillar design that achieves an optimal stress distribution. This has included optimization of the mushroomtip thickness to eliminate the edge singularity [18] as well as the use of a mushroom-shaped pillar with an angled tip [24]. However, these efforts were based on parametric studies and thus did not explore the full design space. Various design optimization frameworks have been developed to explore larger design spaces to determine optimal shapes [28] and surface textures [29], for example. Design optimization and machine learning techniques provide new opportunities for the design of structures with optimal adhesion [30,31]. Recently, Kim et al. [32] and Son et al. [33] applied machine learning techniques to determine the optimal shape of adhesive pillars. In this letter, we determine the optimal pillar geometry via a gradient-based optimization approach and experimentally evaluate the designs.

The goal of this study is to maximize the effective adhesion strength of single fibril contacts through geometric optimization of the fibril shape to control the stress distribution and strain energy release rate at the adhered interface. This is achieved through a gradient-based design optimization framework. The

^{*} Corresponding author. E-mail address: kturner@seas.upenn.edu (K.T. Turner).

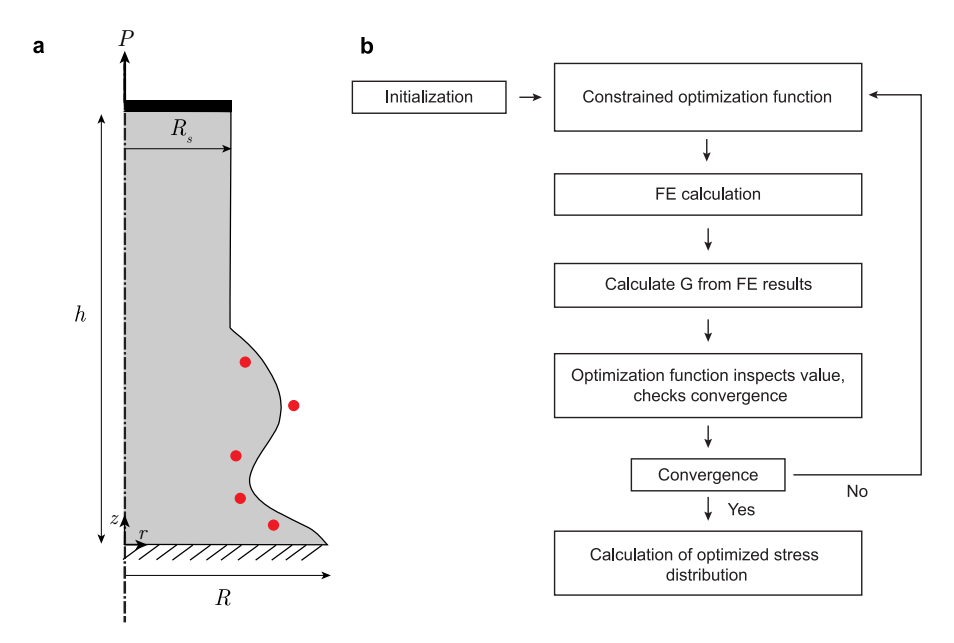


Fig. 1. (a) Schematic of an arbitrary axisymmetric pillar geometry with radius *R* and stalk radius *R*_s, adhered to a rigid substrate. The Bézier control points are shown as red points. Note that the Bézier curve does not pass through the control points, but its shape is determined by them. (b) The workflow of the optimization scheme. (For interpretation of the references to color in this figure legend, the reader is referred to the web version of this article.)

shape of the pillar is defined by a fixed number of control points, and the coordinates of these points are determined by a minimization function (Fig. 1a). The framework consists of a constrained minimization function, which minimizes an objective function that is calculated through finite element (FE) analysis of the parameterized pillar geometry. Optimized pillar geometries and their interfacial stress distributions were determined for pillars with various stalk diameters and compared. Elastomer adhesive pillars (mm-scale) were fabricated based on the optimized designs and their performance was evaluated.

2. Methods

Ideally, the analytic form of the function to be minimized is known, and the gradient can be calculated directly, resulting in quick identification of local minima in optimization schemes. However, in this problem there is no simple analytical relationship between the shape of the pillar and the stress distribution and strain energy release rate at the interface. Thus, the finite difference method is used to calculate gradients. Each function evaluation calls an FE analysis to calculate the stresses at the interface. The objective function is then evaluated using this information, and the coordinates of the control points are adjusted to minimize the objective function. The convergence criteria are checked after each iteration, and the optimization routine is terminated when the convergence criteria are met. Constraints were imposed on the design parameters (i.e. the radial positions of the control points) to limit their range between the stalk radius and the radius of the pillar. This is done to prevent unrealistic geometries that are difficult to fabricate. The optimization framework was constructed in MATLAB, with the constrained non-linear optimization function fmincon from the Optimization Toolbox [34]. This function uses the interior-point method [35] to calculate gradients. No equality or inequality constraints were used. The initial point assumed is the midpoint between the stalk radius and the radius of the pillar, which are the lower and upper bounds of the design variables. Optimization hyperparameters, including step-size, optimality criteria and convergence tolerance, were chosen on a case-by-case basis, depending upon the stalk radius (R_s) of the pillar being optimized to avoid the scheme stalling in the initial few iterations.

2.1. Finite element model

Finite element modeling (ABAQUS 2018, Providence, RI) was used to calculate the stress distribution and the strain-energy release rate for each pillar geometry. The pillars were modeled as a two-dimensional axisymmetric problem, with the pillar height-to-radius ratio fixed at h/R=2. This ratio was chosen because the height does not affect the interface stress distribution for $h \geq 2R$ [21]. The material was assumed to be linear elastic with Young's modulus E=2 MPa and Poisson ratio $\nu=0.49$, representative of polydimethylsiloxane (PDMS). The model presented here is linear elastic, therefore, only these two material parameters are necessary. While PDMS does exhibit non-linear behavior at high strains, the dry adhesion of PDMS to other surfaces is weak leading to strains at failure (Fig. S5, Supplementary Information) that are well below the linear elastic limit of PDMS, which is quite high at approximately 40% strain [36].

To perform pillar shape optimization, the FE script accepts design parameters as arguments and generates a pillar geometry (Fig. 1(a)). The design parameters are the control points (red points in Fig. 1(a)) of a Bézier curve [37], the shape of which is defined by the coordinates of the control points. This approach is chosen because it results in smooth and, in general, manufacturable shapes. This method also reduces the likelihood of meshing errors arising due to complicated geometries with sharp features. For all of the results shown here, five control points were used with coordinates $[(r_1, 0.1R), (r_2, 0.2R), (r_3, 0.4R), (r_4, 0.6R),$ $(r_5, 0.8R)$]. Two points are placed close to the interface as they will have the strongest influence on how stress is distributed at the interface. The endpoints of the Bézier curve were the tip of the pillar (R, 0) and the base of the pillar stalk (R_s, R) . The geometry is only varied over half of the pillar via the Bézier curve, as the interfacial stress only weakly depends on the geometry of the upper part of the pillar (z > R). The model is meshed with linear axisymmetric elements. An average element size of 0.01R was used in all simulations, corresponding to approximately 20,000–30,000 elements per model. The element size was determined through a convergence study (e.g., Fig. S3, Supplementary Information). Both quadrilateral and triangular hybrid elements CAX4RH and CAX3RH were used to mesh the model. The lower edge of the

pillar was fixed to simulate no-slip adhesion to a rigid substrate. The nodes on the top of the pillar were coupled and displaced upwards by 0.02R, generating tensile stresses at the interface. These stresses were calculated and normalized by the average stress at the interface, which is calculated as $\sigma_{zz-avg} = \frac{1}{A} \int_A \sigma_{zz} dA$, where A is the interfacial area. The net force P applied at the top of the pillar is calculated by summing the reaction forces on all of the nodes on the top boundary ($\sigma_{zz-avg} = P/A$ by equilibrium).

2.2. Objective function

The dominant factors that control the detachment load are the presence of defects, the stress singularity at the edge [38], and the uniformity of the interface stress distribution. To design pillars based on these factors in an optimization scheme, three objective functions were considered. (1) Edge singularity strength: The analytical form of the edge stress singularity was used by Balijepalli et al. [19] to quantify the adhesion enhancement in mushroom-shaped pillars relative to a fibril with a simple cylindrical geometry. The strength of this edge singularity is a good candidate for the objective function, however for the comparison between different geometries to be valid, the contact angle between the pillar and surface must be the same, as the order of the singularity changes with the contact angle [39]. (2) Stress uniformity: To obtain a uniform stress distribution, an objective function that is equal to the variance of the stress from the mean stress is the most direct approach. However, the stress distribution obtained via this objective function is sensitive to defects at the edge (Fig. S6, Supplementary Information). (3) Strain energy release rate G of a crack at the pillar edge: The G is a function of both the size of crack/defect and the local stress at the crack. G was calculated through the virtual crack closure technique [40], for an edge crack with length a = 0.02R. By minimizing G, the optimization scheme returns geometries with lower driving forces for interface delamination. Note, we are able to use a simple linear elastic fracture mechanics criterion based on G rather than a more complex cohesive zone representation of adhesion because the combination of adhesive/elastic properties and size of the structures here is known to lead to fracturedominated rather than strength-dominated failures. Specifically, previous work [41] has shown that dry-adhered PDMS pillars will delaminate in a fracture-dominated manner if the pillar radius is greater than $R \approx 0.2 \,\mu\text{m}$.

The third objective function based on G was chosen for the design optimization studies because it allowed the effects of edge defects to be included and did not require a fixed contact angle as the edge singularity method does.

2.3. Experimental methods

To evaluate the performance of the optimized pillar designs. millimeter-scale pillars were fabricated using the two-step molding process outlined in Fig. S1 (Supplementary Information). Simple cylindrical pillars for the control experiments (R = 1.5 mm, H = 3 mm) and optimized Bézier pillars with the same base radius and height were machined from brass on a lathe to make a mold. To avoid rounding due to the tool radius at the tip of the pillars, the pillars were machined with 5 mm of additional height and inserted into a second piece with holes of the same radius, through an interference fit. This machined mold was then treated with trichloro(1H,1H,2H,2H-perflurooctyl) silane (Sigma-Aldrich, St.Louis, MO) to facilitate release. A reverse mold was then fabricated using PDMS (Sylgard 184, Dow Corning Corporation, Midland, MI) with a 5:1 weight ratio of base elastomer to curing agent. This mold was cured in an oven at 85 °C for 4 h. This PDMS mold was silane-treated, attached to a glass slide, and filled

with 10:1 PDMS to mold the pillars. Air-bubbles were removed by placing the filled mold in a vacuum chamber and the PDMS was cured using the parameters noted earlier. The pillars were then removed from the mold.

Pull-off adhesion tests on individual pillars were performed using a custom mechanical test system comprised of a steppermotor driven translation stage (Aerotech Inc., Pittsburgh, USA), a load cell with a full-scale range of 20 N (Cooper Instruments and Systems, Warrenton, VA), and a tip-tilt stage for alignment. The force-displacement data was recorded via a DAQ (NI USB-6211, National Instruments, Austin, TX) interfaced through LabVIEW (National Instruments, Austin, TX). To perform a pull-off test, a glass slide attached to the translation stage was brought into contact with the contact surface of the adhesive pillar, at a speed of 10 μ m/s. The slide was aligned to the pillar using the tilttip stage, through observation of the nature of crack propagation upon pull-off. A well-aligned pillar will have axisymmetric crack propagation. The adhesive interface was imaged through the glass slide using a $2.5 \times$ objective mounted on a tube microscope connected to a CMOS (1024 × 1280) camera (Pixelink A741, Ottawa, Canada). A preload of 300 mN (average contact pressure of 42.4 kPa) was applied in all tests to ensure conformal contact. This preload was held for 30 s, and then the glass slide was retracted at a speed of 10 μ m/s. The peak tensile force during retraction is recorded as the pull-off force of the pillar specimen.

3. Results and discussion

3.1. Simulations

The results of the geometric optimization are summarized in Fig. 2. Optimized pillar designs for stalk radii $R_s = 0.5R$, 0.8R and the stress distributions at the interface of each design under an applied normal force are shown, along with the evolution of the normalized objective function $\tilde{G} = GER^3/P^2$ for each geometry during the optimization process (Fig. 2(c)). \tilde{G} as function of crack length, a/R, for the these designs is shown in Fig. S2, (Supplementary Information). In all cases, \tilde{G} increases with crack length suggesting that it is appropriate to optimize based on G at the edge (i.e. G at a short crack length of 0.02R). For the case of the cylindrical pillar, there is a stress singularity at the edge that significantly reduces the effective adhesion strength (Fig. 2(b)). The stress distributions for the optimized pillars are free from singularities and the stress decreases monotonically as it approaches the edge. The stress distribution for the optimal pillar design with $R_s = 0.8R$ is quite similar to that obtained from the machine learning-based model in Kim et al. [32]. While the optimal designs and stress distributions obtained are similar, the gradient-based optimization scheme required 25 iterations (150 FE simulations) while the machine-learning model was trained with 200,000 FE simulations. This illustrates that gradient-based optimization techniques can be quite data-efficient. The absence of a singularity is primarily due to the shape of the pillar profile near the edge in which the contact angle ranged from 40°-45° for the optimized designs. Aksak et al. [24] showed that adhesive pillars with a tip angle of 45° had no singular stresses near the edge, similar to what is observed in these optimized cases. A similar free-form pillar shape was also reported by Son et al. [33] who used a Bayesian optimization approach.

The redistribution of stress in the optimized pillars leads to elevated stresses away from the edge. This is similar to the mushroom and composite pillars. For the case of $R_s=0.8R$, the stress distribution is nearly uniform from the center of the pillar to r=0.9R, followed by a decrease in stress close to the edge. This is a near-ideal stress distribution that is both free of regions of high stress and has low stress in the edge region

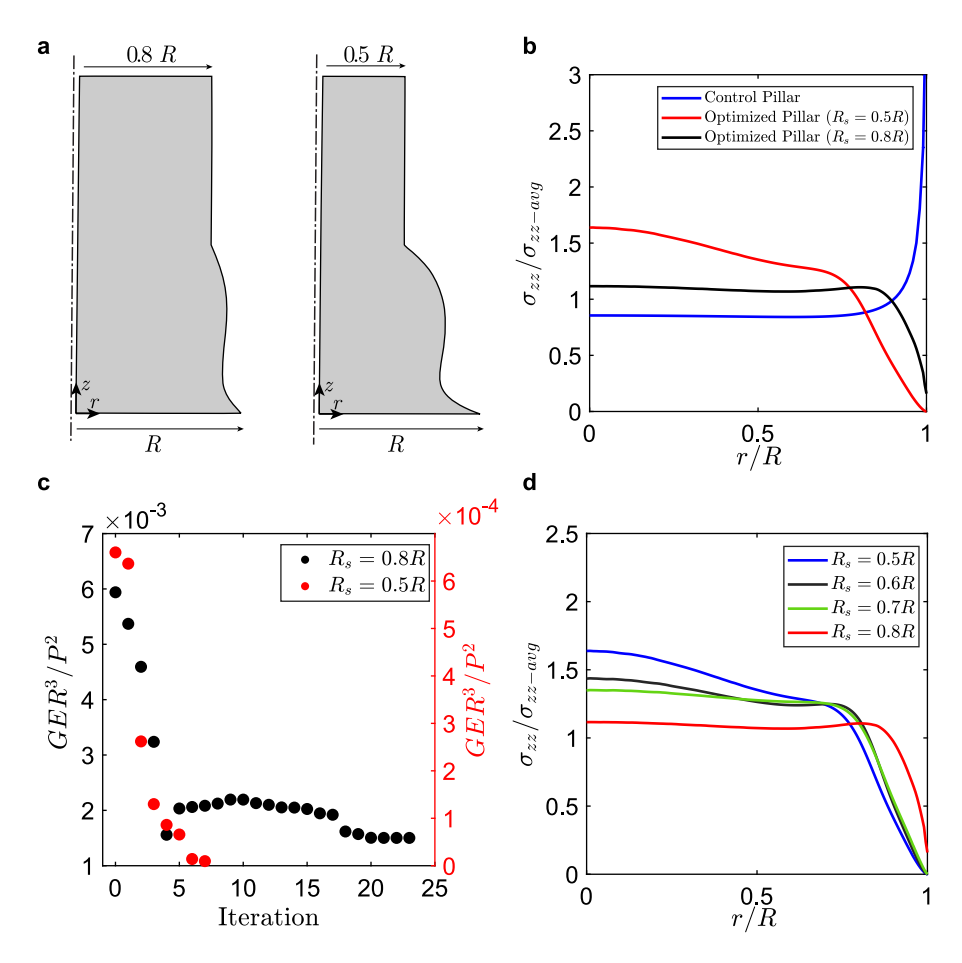


Fig. 2. (a) Optimized pillar geometries for $R_s = 0.5R$, 0.8R. (b) Interface stress distributions of optimized pillars compared to the control pillar (c) Evolution of the normalized objective function \tilde{G} with iteration number for the two cases considered, $R_s = 0.8R$ (black) and $R_s = 0.5R$ (red). (d) Optimal stress distributions obtained for various stalk diameters. (For interpretation of the references to color in this figure legend, the reader is referred to the web version of this article.)

where defects are likely to be present. Geometric optimization was performed for multiple stalk radii, and as R_s was increased, the stalk transferred more load to and resulted in higher stresses in the central region of the pillar (Fig. 2(d)).

As the stress in the central region increases, the probability of failure from an edge crack decreases, and it becomes more likely that detachment will initiate in the center. Whether or not detachment initiates in the center is determined by the stress in this region as well as the size of defects. The optimization was repeated with an objective function of $f_{objective} = (G_{edge} + G_{center})$, considering two defects of equal size at the center and the edge. The optimized result had a lower stress at the center of the pillar compared to the case optimized for an edge crack alone, although the change was small (\sim 3% reduction in the stress at the center). However, the results depend strongly on the size of the defect at the center. If a larger center crack is assumed, the optimization scheme will result in a design that has lower stress in the center region. The sensitivity of the design to Poisson's ratio was also studied, with the optimal geometry and stress distribution being nominally unchanged for ν from 0.45 to 0.49, which encompasses the typical range of Poisson's ratios for elastomers.

The optimized pillar designs in this work are compared to previous designs reported in the literature. Stress distributions for several different reported geometries were calculated via FE and are compared in Fig. 3(a).

The two benchmark geometries used for comparison are the mushroom geometry and the angled-tip geometry, schematics of which are shown in Fig. 3(b) and (c) respectively. The mushroom geometry has a stalk radius of $R_s = 0.5R$ and tip-thickness of

0.2R, based on work by Carbone et al. [18,42]. The angled-tip geometry was adapted from Aksak et al. [24], with a tip-angle of 45° and $R_s = 0.8R$, in order to compare it with the optimized designs in this study. Note the different ways in which these geometries redistribute stress. In the mushroom design, there is a high stress (3× the average) at the center of the pillar, while the angled-tip pillar has a near-uniform stress distribution. Assuming a uniform defect size across the interface, center crack initiation is more likely in both cases. The angled-tip pillar is expected to have a higher pull-off force due to lower peak stress in the central region.

The optimal pillar design in the present work ($R_s = 0.8R$), when compared to the angled-tip design, has an 8% lower stress from r = 0 to r = 0.7R, and a lower stress in the near-edge region as $r \rightarrow R$. Therefore, for both center and edge crack initiation, the optimal design should have higher pull-off forces For small values of stalk radii like $R_s = 0.5R$, it is most appropriate to compare the results to the mushroom geometry with the same R_s . The optimal design has a more uniform stress distribution and no edge singularity, which is expected to lead to higher adhesive load capacity.

3.2. Experiments

PDMS pillars (mm-scale) with three geometries were fabricated: the two optimized designs with stalk radii of $R_s = 0.5R$, 0.8R and a cylindrical pillar as a control. R = 1.5 mm for all pillars. Adhesive pull-off experiments were performed on these pillars. The mm-scale pillars are used to allow for optical imaging

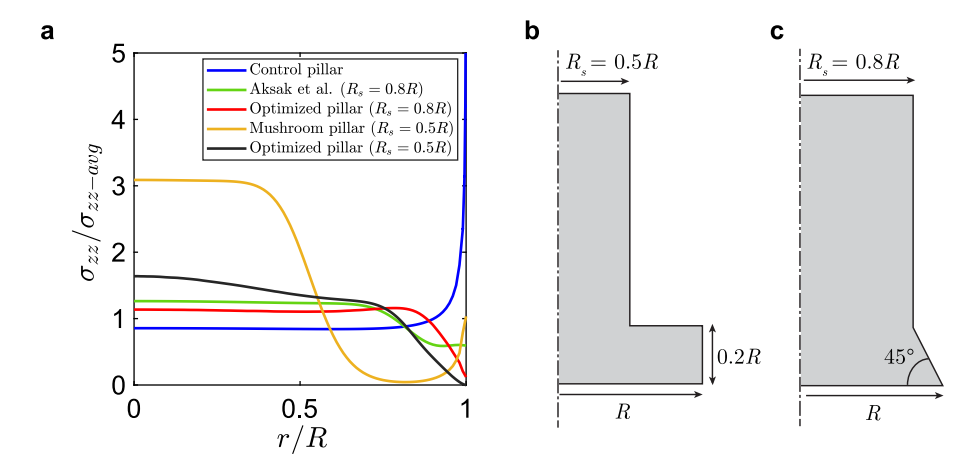


Fig. 3. (a) Comparison of optimized pillar stress distributions to previously reported pillar geometries. (b) Mushroom pillar geometry with tip thickness = 0.2R. (c) Angled-tip pillar geometry proposed by Aksak et al. [24] with tip-angle of 45° .

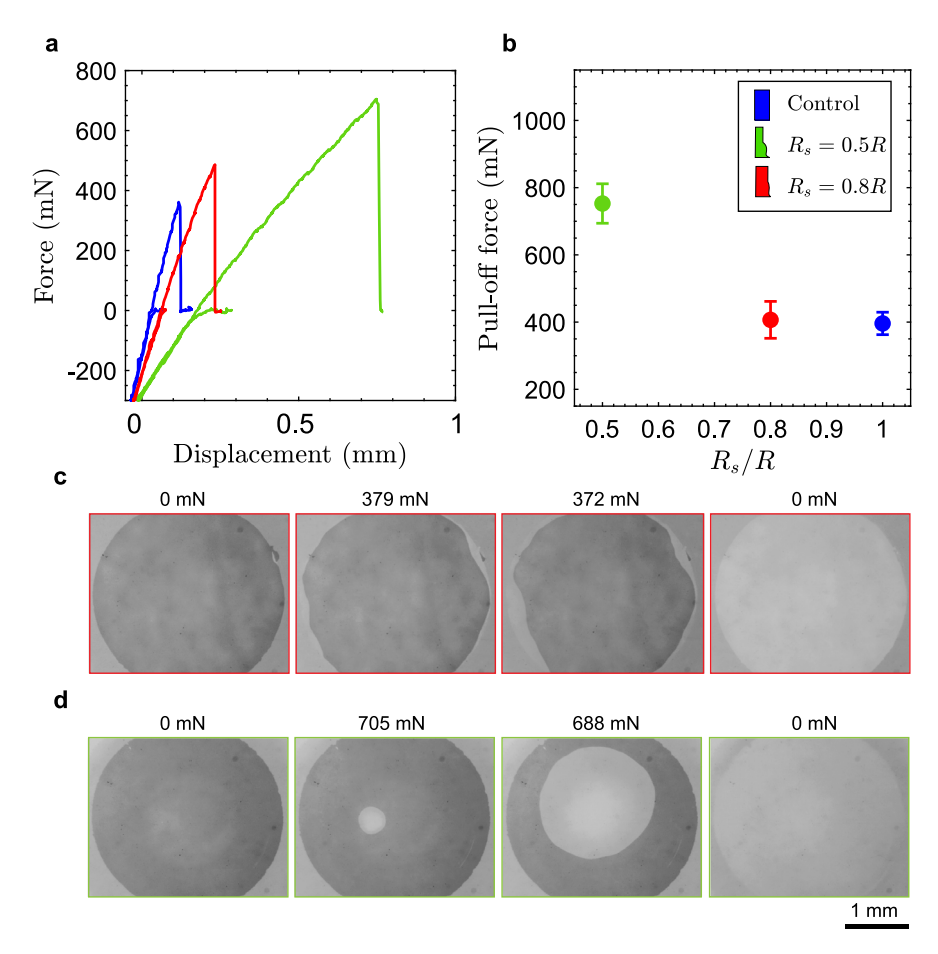


Fig. 4. (a) Representative force–displacement curves for pull-off tests of each pillar geometry. (b) Average pull-off force for each pillar geometry. Each data point is the average of 5 measurements and the error bars represent the standard deviation. (c) Images of interface crack propagation initiating from the edge for $R_s = 0.8R$. (d) Images of interface crack propagation for the control pillar are shown in Fig. S4, Supplementary Information.

of crack initiation and propagation during the experiment; such observations are difficult in micron-scale pillars like those studied by Son et al. [33]. Representative force–displacement data and average pull-off forces for each geometry are shown in Fig. 4(a) and (b), which shows that the optimized design with $R_s = 0.5R$ has the best adhesive performance, with an average pull-off force almost twice of that of the control pillar. The optimized pillar with $R_s = 0.8R$ shows little adhesion enhancement, with an average pull-off force nearly the same as the control pillar. Note

that the stiffness of the pull-off curve decreases as $R_{\rm s}$ of the pillar is reduced. This is a potential advantage as the higher compliance will require a lower preload to achieve conformal contact if these pillars are fabricated in an array. Also, notably, the displacement to full detachment for this pillar from the substrate is three times greater than the case of $R_{\rm s}=0.8R$ and the area under the force-displacement curve is also larger. This is a significant advantage, as this design has both increased adhesive strength and energy dissipation.

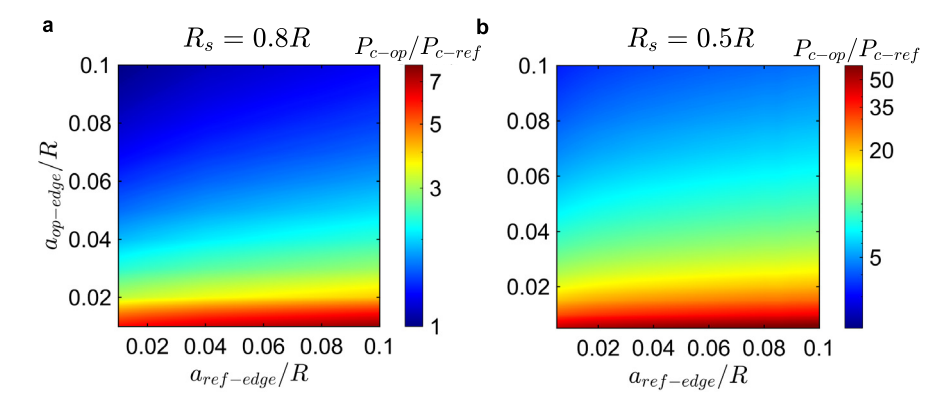


Fig. 5. (a) Normalized pull-off force as a function of the length of edge cracks of the cylindrical punch $(a_{ref-edge})$ and the optimized pillar $(a_{op-edge})$ for optimized pillar of stalk radius $R_s/R = 0.8$. (b) Normalized pull-off force as a function of center crack length of the optimized pillar $(a_{op-edge})$ and the edge crack lengths of the cylindrical punch $(a_{ref-edge})$ for optimized pillar of stalk radius $R_s/R = 0.5$. Both colormaps are shown in a log scale for clarity. (For interpretation of the references to color in this figure legend, the reader is referred to the web version of this article.)

The location of crack initiation and the progression of the crack front is important in understanding the adhesive behavior of the pillar. For the control pillar, the crack front initiates at the edge and then progresses in a near-axisymmetric manner. For the optimized pillars, in the $R_s=0.8R$ case, edge crack initiation is observed, and for the $R_s=0.5R$ pillar, center crack initiation was observed. Sequential images of interface crack initiation and propagation for both the center and edge cases are shown in Fig. 4(c) and (d). The shift of crack initiation from the edge to the center for the case of $R_s=0.5R$ is due to the low near-edge stresses in the optimized stress distribution.

The modeling results suggest that the optimized pillar with $R_{\rm s} = 0.8R$ should also fail via a center crack, because of the absence of the stress singularity and the near-uniform stress distribution. This is clearly not the case and is likely due to the limited accuracy of the machined pillar mold and the pillar fabrication technique. In the case of $R_s = 0.8R$, the contours of the pillar are subtle and may not be faithfully replicated in the machining and molding process. For the stress singularity to vanish, the contact angle at the edge should be well-defined and sharp. However, due to manufacturing, slightly rounded edges are obtained. This results in a sub-optimal geometry and stress distribution, decreasing the adhesive strength, as observed by Aksak et al. [24]. A highly accurate fabrication technique, such as two-photon lithography, may be able to overcome these challenges and allow for the fabrication of optimized pillar shapes with higher adhesion strength.

3.3. Defect sensitivity

The presence of defects or cracks at the interface significantly influences the degree of adhesion enhancement. To understand this effect, the adhesion enhancement ratio P_{c-op}/P_{c-ref} of an optimized pillar relative to the reference control pillar is shown as a function of the crack length at the interface of the optimized pillar (a_{op}) and the control pillar (a_{ref}) in Fig. 5. This ratio is calculated from the normalized FE-calculated strain energy release rate values:

$$P_{c-op}/P_{c-ref} = (\tilde{G}_{ref}/\tilde{G}_{op})^{1/2}$$
(1)

By calculating an adhesion enhancement ratio, we avoid the need to assume a critical strain energy release rate G_c , which for PDMS-glass can vary with test conditions. A similar approach was adopted by Luo & Turner to understand the location of interface failure in transfer printing [43]. Further details of this approach can be found in the Supplementary Information.

Fig. 5(a) shows P_{c-op}/P_{c-ref} for the optimized pillar with $R_s = 0.8R$. The defect size may vary between the optimized and control

pillars, therefore a contour plot is used to show the effect of various crack length combinations. The cracks considered here are edge cracks, as this is the failure mode seen in experiments for the optimized pillar with $R_s = 0.8R$ and the control pillar. The largest enhancement is obtained for the smallest defect sizes, and $P_{c-op}/P_{c-ref} \rightarrow 1$ for optimal pillars with larger defect sizes, showing that it is difficult to achieve enhancement unless the defect sizes in the optimized pillars are small. In the case of the optimized pillar with $R_s = 0.5R$, the enhancement ratio is calculated with a range of center cracks in the optimized pillar, and a range of edge cracks in the control pillar, consistent with experimental observations. As is evident in Fig. 5(b), high enhancement ratios (\sim 50×) can be obtained at small defect sizes, however, the enhancement decays quickly as the defect size increases, implying high defect sensitivity. As mentioned before, using a high-precision manufacturing technique like two-photon lithography may result in pillars with smaller defects, potentially leading to better adhesive performance [27].

4. Conclusions

In summary, we report optimal adhesive pillar designs with near-ideal stress distributions obtained via a data-efficient gradient-based geometric optimization scheme. The optimal designs have interface stress distributions with no singularities in the near-edge region, which is often the dominant factor in the failure of adhesive pillars. The designs were also compared to previously reported pillar geometries and the optimized geometries obtained here have stress distributions that are more uniform, with lower peak stresses. These optimized pillars are also free from any sharp corners (e.g. the intersection of the cap and stalk in mushroom pillars), which can lead to failure in use. Experiments on mm-scale pillars with these optimal designs were performed, with an adhesion enhancement of $2\times$ achieved in the optimal design with stalk radius $R_s = 0.5R$. The location of crack initiation was also shifted to the center from the edge region, due to the low stresses at the edge. The essential mechanics of these geometries is expected to hold for pillars at the micrometer scale. in which case the adhesion enhancement is expected to be larger due to lower defect densities. More generally, the geometric optimization scheme implemented in this study can be applied to other systems where the bulk or interface stress distribution can be modified through changes in geometry, improving mechanical performance.

Declaration of competing interest

The authors declare that they have no known competing financial interests or personal relationships that could have appeared to influence the work reported in this paper.

Data availability

Data will be made available on request.

Acknowledgments

This work was supported by the National Science Foundation, United States under award CMMI-1663037 and CMMI-1830475. We thank Aoyi Luo and Gnana Saurya Vankalayapati for helpful discussion and technical input. We also thank Peter Szczesniak and Jason Pastor for precision machining the pillar molds.

Appendix A. Supplementary data

Supplementary material related to this article can be found online at https://doi.org/10.1016/j.eml.2023.101969.

References

- R. Hensel, K. Moh, E. Arzt, Engineering micropatterned dry adhesives: From contact theory to handling applications, Adv. Funct. Mater. 28 (28) (2018) 1800865. http://dx.doi.org/10.1002/adfm.201800865.
- [2] J. Shintake, V. Cacucciolo, D. Floreano, H. Shea, Soft robotic grippers, Adv. Mater. 30 (29) (2018) 1707035, http://dx.doi.org/10.1002/adma. 201707035.
- [3] M.T. Pope, C.W. Kimes, H. Jiang, E.W. Hawkes, M.A. Estrada, C.F. Kerst, W.R.T. Roderick, A.K. Han, D.L. Christensen, M.R. Cutkosky, A multimodal robot for perching and climbing on vertical outdoor surfaces, IEEE Trans. Robot. 33 (1) (2017) 38–48, http://dx.doi.org/10.1109/TRO.2016.2623346.
- [4] E.W. Hawkes, E.V. Eason, A.T. Asbeck, M.R. Cutkosky, The Gecko's Toe: Scaling directional adhesives for climbing applications, IEEE/ASME Trans. Mechatronics 18 (2) (2013) 518–526, http://dx.doi.org/10.1109/TMECH. 2012.2209672.
- [5] M. Zhou, Y. Tian, D. Sameoto, X. Zhang, Y. Meng, S. Wen, Controllable interfacial adhesion applied to transfer light and fragile objects by using gecko inspired mushroom-shaped pillar surface, ACS Appl. Mater. Interfaces 5 (20) (2013) 10137–10144, http://dx.doi.org/10.1021/am402815x.
- [6] S. Song, D.-M. Drotlef, J. Paik, C. Majidi, M. Sitti, Mechanics of a pressure-controlled adhesive membrane for soft robotic gripping on curved surfaces, Extreme Mech. Lett. 30 (2019) 100485, http://dx.doi.org/10.1016/j.eml. 2019.100485.
- [7] H.E. Jeong, J.-K. Lee, H.N. Kim, S.H. Moon, K.Y. Suh, A nontransferring dry adhesive with hierarchical polymer nanohairs, Proc. Natl. Acad. Sci. 106 (14) (2009) 5639–5644, http://dx.doi.org/10.1073/pnas.0900323106.
- [8] S. Kim, M. Sitti, Biologically inspired polymer microfibers with spatulate tips as repeatable fibrillar adhesives, Appl. Phys. Lett. 89 (26) (2006) 261911, http://dx.doi.org/10.1063/1.2424442.
- [9] J. Purtov, M. Frensemeier, E. Kroner, Switchable adhesion in vacuum using bio-inspired dry adhesives, ACS Appl. Mater. Interfaces 7 (43) (2015) 24127–24135, http://dx.doi.org/10.1021/acsami.5b07287.
- [10] M.P. Murphy, B. Aksak, M. Sitti, Gecko-inspired directional and controllable adhesion, Small 5 (2) (2009) 170–175, http://dx.doi.org/10.1002/smll. 200801161.
- [11] A. Carlson, H.-J. Kim-Lee, J. Wu, P. Elvikis, H. Cheng, A. Kovalsky, S. Elgan, Q. Yu, P.M. Ferreira, Y. Huang, K.T. Turner, J.A. Rogers, Shearenhanced adhesiveless transfer printing for use in deterministic materials assembly, Appl. Phys. Lett. 98 (26) (2011) 264104, http://dx.doi.org/10.1063/1.3605558.
- [12] A. Carlson, A.M. Bowen, Y. Huang, R.G. Nuzzo, J.A. Rogers, Transfer printing techniques for materials assembly and micro/nanodevice fabrication, Adv. Mater. 24 (39) (2012) 5284–5318, http://dx.doi.org/10.1002/adma. 201201386.
- [13] M.A. Meitl, Z.-T. Zhu, V. Kumar, K.J. Lee, X. Feng, Y.Y. Huang, I. Adesida, R.G. Nuzzo, J.A. Rogers, Transfer printing by kinetic control of adhesion to an elastomeric stamp, Nature Mater. 5 (1) (2006) 33–38, http://dx.doi.org/ 10.1038/nmat1532.
- [14] H.-J. Kim-Lee, A. Carlson, D.S. Grierson, J.A. Rogers, K.T. Turner, Interface mechanics of adhesiveless microtransfer printing processes, J. Appl. Phys. 115 (14) (2014) 143513, http://dx.doi.org/10.1063/1.4870873.
- [15] K. Autumn, M. Sitti, Y.A. Liang, A.M. Peattie, W.R. Hansen, S. Sponberg, T.W. Kenny, R. Fearing, J.N. Israelachvili, R.J. Full, Evidence for van der Waals adhesion in gecko setae, Proc. Natl. Acad. Sci. 99 (19) (2002) 12252–12256, http://dx.doi.org/10.1073/pnas.192252799.
- [16] S.N. Gorb, Smooth attachment devices in insects: functional morphology and biomechanics, Adv. Insect Physiol. 34 (2007) 81–115.

- [17] H. Gao, X. Wang, H. Yao, S. Gorb, E. Arzt, Mechanics of hierarchical adhesion structures of geckos, Mech. Mater. 37 (2–3) (2005) 275–285, http://dx.doi.org/10.1016/j.mechmat.2004.03.008.
- [18] G. Carbone, E. Pierro, S.N. Gorb, Origin of the superior adhesive performance of mushroom-shaped microstructured surfaces, Soft Matter 7 (12) (2011) 5545, http://dx.doi.org/10.1039/c0sm01482f.
- [19] R. Balijepalli, M. Begley, N. Fleck, R. McMeeking, E. Arzt, Numerical simulation of the edge stress singularity and the adhesion strength for compliant mushroom fibrils adhered to rigid substrates, Int. J. Solids Struct. 85–86 (2016) 160–171, http://dx.doi.org/10.1016/j.ijsolstr.2016.02.018.
- [20] A. del Campo, C. Greiner, E. Arzt, Contact shape controls adhesion of bioinspired fibrillar surfaces, Langmuir 23 (20) (2007) 10235–10243, http: //dx.doi.org/10.1021/la7010502.
- [21] H.K. Minsky, K.T. Turner, Achieving enhanced and tunable adhesion via composite posts, Appl. Phys. Lett. 106 (20) (2015) 201604, http://dx.doi. org/10.1063/1.4921423.
- [22] H.K. Minsky, K.T. Turner, Composite microposts with high dry adhesion strength, ACS Appl. Mater. Interfaces 9 (21) (2017) 18322–18327, http://dx.doi.org/10.1021/acsami.7b01491.
- [23] R.G. Balijepalli, S.C. Fischer, R. Hensel, R.M. McMeeking, E. Arzt, Numerical study of adhesion enhancement by composite fibrils with soft tip layers, J. Mech. Phys. Solids 99 (2017) 357–378, http://dx.doi.org/10.1016/j.jmps. 2016 11 017
- [24] B. Aksak, K. Sahin, M. Sitti, The optimal shape of elastomer mushroom-like fibers for high and robust adhesion, Beilstein J. Nanotechnol. 5 (2014) 630–638, http://dx.doi.org/10.3762/bjnano.5.74.
- [25] S.C.L. Fischer, K. Groß, O. Torrents Abad, M.M. Becker, E. Park, R. Hensel, E. Arzt, Funnel-shaped microstructures for strong reversible adhesion, Adv. Mater. Interfaces 4 (20) (2017) 1700292, http://dx.doi.org/10.1002/admi. 201700292
- [26] Y. Wang, V. Kang, E. Arzt, W. Federle, R. Hensel, Strong wet and dry adhesion by cupped microstructures, ACS Appl. Mater. Interfaces 11 (29) (2019) 26483–26490, http://dx.doi.org/10.1021/acsami.9b07969.
- [27] H. Gao, H. Yao, Shape insensitive optimal adhesion of nanoscale fibrillar structures, Proc. Natl. Acad. Sci. 101 (21) (2004) 7851–7856, http://dx.doi. org/10.1073/pnas.0400757101.
- [28] X. Wang, L. Shi, Q. Dai, W. Huang, X. Wang, Multi-objective optimization on dimple shapes for gas face seals, Tribol. Int. 123 (2018) 216–223.
- [29] C. Shen, M. Khonsari, Texture shape optimization for seal-like parallel surfaces: theory and experiment, Tribol. Trans. 59 (4) (2016) 698-706.
- [30] A. Luo, K.T. Turner, Achieving enhanced adhesion through optimal stress distributions, J. Mech. Phys. Solids 156 (2021) 104610.
- [31] A. Luo, H. Zhang, K.T. Turner, Machine learning-based optimization of the design of composite pillars for dry adhesives, Extreme Mech. Lett. 54 (2022) 101695.
- [32] Y. Kim, C. Yang, Y. Kim, G.X. Gu, S. Ryu, Designing an adhesive pillar shape with deep learning-based optimization, ACS Appl. Mater. Interfaces 12 (21) (2020) 24458–24465, http://dx.doi.org/10.1021/acsami.0c04123.
- [33] D. Son, V. Liimatainen, M. Sitti, Machine learning-based and experimentally validated optimal adhesive fibril designs, Small (2021) 2102867., http://dx.doi.org/10.1002/smll.202102867.
- [34] MATLAB, Version 9.7.0 (R2019b), The MathWorks Inc., Natick, Massachusetts, 2019.
- [35] R.H. Byrd, J.C. Gilbert, J. Nocedal, A trust region method based on interior point techniques for nonlinear programming, Math. Program. 89 (1) (2000) 149–185.
- [36] F. Schneider, T. Fellner, J. Wilde, U. Wallrabe, Mechanical properties of silicones for MEMS, J. Micromech. Microeng. 18 (6) (2008) 065008.
- [37] M.E. Mortenson, Mathematics for Computer Graphics Applications, Industrial Press Inc., 1999.
- [38] A. Spuskanyuk, R. McMeeking, V. Deshpande, E. Arzt, The effect of shape on the adhesion of fibrillar surfaces, Acta Biomater. 4 (6) (2008) 1669–1676, http://dx.doi.org/10.1016/j.actbio.2008.05.026.
- [39] A. Akisanya, N. Fleck, Interfacial cracking from the freeedge of a long bi-material strip, Int. J. Solids Struct. 34 (13) (1997) 1645–1665, http://dx.doi.org/10.1016/S0020-7683(96)00053-4.
- [40] R. Krueger, Virtual crack closure technique: History, approach, and applications, Appl. Mech. Rev. 57 (2) (2004) 109–143, http://dx.doi.org/10.1115/1.1595677.
- [41] Y. Jiang, D.S. Grierson, K.T. Turner, Flat punch adhesion: transition from fracture-based to strength-limited pull-off, J. Phys. D: Appl. Phys. 47 (32) (2014) 325301.
- [42] G. Carbone, E. Pierro, Sticky bio-inspired micropillars: Finding the best shape, Small 8 (9) (2012) 1449–1454, http://dx.doi.org/10.1002/smll. 201102021.
- [43] A. Luo, K.T. Turner, Mechanics of crack path selection in microtransfer printing: Challenges and opportunities for process control, J. Mech. Phys. Solids 143 (2020) 104066.